Signatures of the long-range phase transition in topological Josephson junctions

Jun-Tong Ren,[1] Sha-Sha Ke,[1] Yong Guo,[2] Huai-Wu Zhang,[1] and Hai-Feng Lü[1,2,*]

[1]*School of Physics and State Key Laboratory of Electronic Thin Films and Integrated Devices, University of Electronic Science and Technology of China, Chengdu 610054, China*

[2]*Department of Physics and State Key Laboratory of Low-Dimensional Quantum Physics, Tsinghua University, Beijing 100084, China*

(Received 10 August 2022; revised 10 October 2022; accepted 14 October 2022; published 31 October 2022)

The extended Kitaev models spark a recent surge of interest due to its unprecedented topological phase with fractional invariants. In this extended model of topological superconductors, long-range pairing interactions can induce a pair of subgap massive edge modes (MEMs), posing novel challenges to the unambiguous detection of Majorana bound states (MBSs) sustained by the same model in the short-range limit. Here we investigate the effect of a power-law decayed long-range pairing on the dc and ac Josephson currents between two Majorana nanowires. By varying the magnetic field and long-range pairing, the nanowires can be driven into different phases hosting MEMs, MBSs, or trivial Andreev bound states (ABSs), which considerably modulate the Josephson current. For weakly linked Josephson junctions, we show that the MEMs emerging in the long-range phases can induce a zigzag profile in the dc current-phase relation featured by two sign reversals deviating from the point where the superconducting phase difference $\phi = \pi$. In contrast, the Josephson current indicates a sharp sign reversal at $\phi = \pi$ in the short-range phase that hosts MBSs, while a smooth sinelike dc Josephson current appears in the presence of ABSs. In the nonequilibrium junction biased by a voltage, we identify a 4π ac Josephson current in the short-range phases, indicating a MBSs-mediated tunneling process dominating the supercurrents. Differently, when the system enters MEMs-hosted long-range phases, the ordinary ac Josephson current with 2π periodicity can be restored. In addition, we find the ac Josephson current induced by MEMs is significantly suppressed under the strong long-range pairing interactions. These signatures can serve as probes to discriminate MBSs from MEMs and ABSs.

DOI: 10.1103/PhysRevB.106.165428

I. INTRODUCTION

Majorana bound states (MBSs) in the topological superconductors have attracted decade-long studies in the condensed matter physics [1–5]. This emerging topological phase of matter is expected to be an building block for fault-tolerant topological quantum computation due to its non-Abelian statistics [6–10]. Although many experimental researches have reported signatures of MBSs so far [11–18], those results are inconclusive and a decisive evidence of their existence has not been revealed yet [19–21]. In the hybrid superconductor-semiconductor nanowires, a stringent probe for the elusive MBSs can be established by measuring the fractional Josephson effect through a Josephson junction between two topological superconducting nanowires. This phenomenon was proposed to demonstrate an anomalous 4π periodicity in the superconducting phase difference $\phi = \phi_1 - \phi_2$ between the two wires with zero bias compared to the ordinary 2π periodicity measured in a conventional Josephson junction [1,22–29].

Theoretically, the equilibrium supercurrents induced by fractional Josephson effects (dc Josephson currents) with 4π periodicity can be observed if the fermion parity is preserved during the phase evolution [4]. This permits a protected MBSs-mediated crossing at $\phi = \pi$ which prevents the system evolving adiabatically back to the ground state as ϕ evolves from 0 to 2π, unlike for other trivial zero-energy states [30]. However, realistic Josephson junctions are often composed by two topological superconducting nanowires with finite lengths. The finite-size effect will give rise to additional MBSs at the two far ends of the Josephson junction, allowing for finite hybridizations of MBSs on each nanowire even when the fermion parity is preserved. This hybridization leaves residual energy splittings at $\phi = \pi$ which inevitably destroys the measurements of fractional Josephson effects as the system stays in the ground state during the whole phase evolution [31]. The anomalous periodicity can be recovered via Landau-Zener transition with a voltage bias applied to Josephson junction [32]. The Landau-Zener transition assists nonadiabatic transitions between states of the same fermion parity, resulting in an ac Josephson current with a bias-dependent 4π-periodic tunneling regime [33]. Therefore, the fractional Josephson effects can still provide a measurable probe for the existence of MBSs in realistic Josephson junction experiments [34,35].

Recent experimental progress facilitates the fine-tuning of the interactions between particles in the quantum systems, pushing the long-range interacting studies from the theoretical investigations to the practical applications [36,37]. A novel quantum phase induced by the long-range effect with power-law decaying pairing interactions in the extended Kitaev chain has raised great concern [38–49]. This long-range pairing profile often takes a form of $\Delta_{ij} = \Delta r_{ij}^{-\alpha}$ where Δ is the pairing energy between the nearest-neighboring sites, r_{ij} is the

*lvhf04@uestc.edu.cn

spatial distance from site i to j, and the exponent α describes the decaying rate. Among other features, the long-range quantum phase ($\alpha < 1$) is characterized by a pair of massive edge modes (MEMs) hybridizing finitely even in the thermodynamic limit [50–53], unlike the exponentially decaying MBSs in the short-range regime ($\alpha \gg 1$). It is thus important to discriminate MBSs from MEMs appearing in the long-range phase in a realistic device.

The long-range effects have also been intensively explored in various realistic systems. The long-range superconductivity has been experimentally observed in the magnetic impurity chains on superconducting substrates where the large spatial extent of slowly decayed Shiba states results in the long-range couplings between the magnetic impurities [54–58]. The steady Floquet-Andreev states have been generated in a Josephson junction by continuous microwave application [59], which offers an ideal platform for realizing the Floquet engineering of long-range superconductivity via driven tunneling interactions [60,61]. Besides condensed matter systems, electric circuits recently manifest as an exceptional platform to imitate the long-range tight-binding model by the inductor-capacitor network [62–65], providing an alternative pathway to simulate the long-range superconductivity. Other experimental proposals include engineering the long-range Kitaev chain via planar Josephson junctions [66,67] and manipulating the variable-range interactions in trapped atomic ions [68,69]. For nanowire-based topological superconducting devices, Wang *et al.* develop a low-energy effective theory to capture the long-range superconductivity in the weakly coupled limit [70], which mimics the long-range interactions derived for the magnetic chains on superconductor substrates [71]. A new topological phase featured by MEMs can be identified via fine-tuning a slowly decayed pairing amplitude with long-range interactions falling as $1/r_{ij}^{\alpha}$ [38,72].

In this work, we investigate the influence of long-range pairing interactions on the equilibrium and out-of-equilibrium supercurrents in the Josephson junctions composed of a normal region tunneling coupled to two superconducting regions. The long-range superconducting pairing interaction between two particles is taken as a decaying power-law function of their spatial distance. We start with a continuum model of a single topological superconducting nanowire and present its phase diagram. In the case of a finite-sized system with open boundary condition, the low-lying energy spectra and the wave functions along the whole junction in both long-range and short-range phases are given. It is found that the Josephson current indicates distinct dependence on the superconducting phase difference in the presence MBSs, MEMs, and trivial Andreev bound states (ABSs). For the out-of-equilibrium currents driven by a biased voltage, we show a 4π periodicity of ac Josephson current for MBSs persisting in the short-range limit. Differently, a conventional 2π ac Josephson current appears in the long-range phase hosting MEMs.

The rest of this paper is organized as follows. In Sec. II, we present the model Hamiltonian of the Josephson junction with long-range pairing interactions. For the long-range superconducting region, we give the derivation of its topological invariants and the phase diagram. We then employ the nonequilibrium Greens function method combined with a partition-free approach to outline the calculation of Josephson currents. In Sec. III, the energy spectra and wave functions are examined in a long-range Josephson junction with a finite length. We also discuss the numeric results of Josephson currents and investigate the distinct signatures in the presence of MEMs, MBSs, and ABSs, respectively. Finally, we summarize our results in Sec. IV.

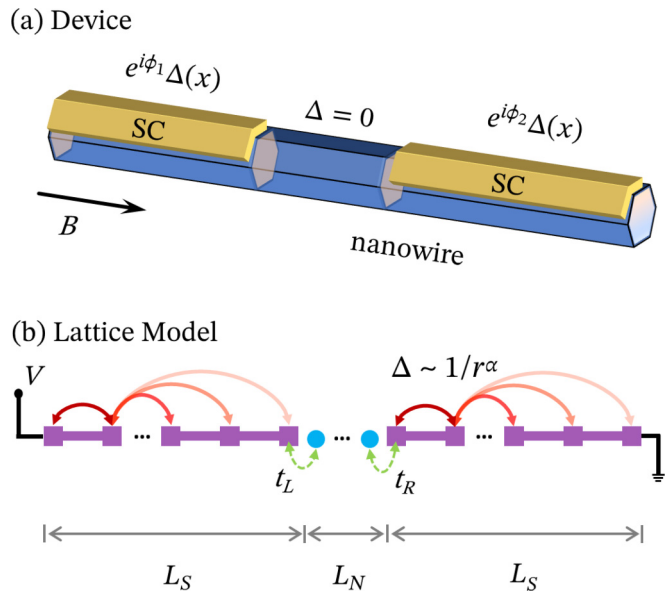

FIG. 1. (a) Schematic view and (b) the corresponding lattice model of the one-dimensional Josephson junction consisting of two superconducting regions and a central normal region with length L_S and L_N. The proximity-induced long-range pairing interactions take a power-law dependence on the spatial distance r and acquire a phase difference $\phi = \phi_1 - \phi_2$ across the junction. The tunneling couplings at the junction interfaces are described by t_L and t_R. The central region can sustain static or nonequilibrium supercurrents when the applied voltage is zero or finitely biased.

II. MODEL AND FORMALISM

We consider a one-dimensional Josephson junction with long-range superconducting pairing interactions represented in Fig. 1. The system Hamiltonian reads

$$H = H_N + H_L + H_R + H_T. \tag{1}$$

Here H_N denotes the Hamiltonian of the central normal region, H_γ with $\gamma \in \{L, R\}$ specify the left and right superconducting regions, and H_T describes the tunneling couplings across the two Josephson junction interfaces, respectively. For a realistic nanowire-based device, the superconducting regions consist of spin-orbit-coupled semiconducting nanowires covered with the superconductor thin films. The long-range superconducting pairing potentials are proximity-induced by two s-wave superconductors. Correspondingly, H_γ can be decomposed into two parts $H_\gamma = H_{\rm NW} + H_{\rm SC}^{\gamma}$

$$H_{\rm NW} = \int_0^{L_S} dx \Psi^{\dagger}(x) \mathcal{H}_{\rm NW} \Psi(x), \tag{2}$$

$$H_{\rm SC}^{\gamma} = \int_0^{L_S} dx dx' \psi_{\uparrow}^{\dagger}(x) \Delta_{\gamma}(x, x') \psi_{\downarrow}(x') + \text{H.c.}, \tag{3}$$

where L_S is the length of the superconducting regions. The Hamiltonian of the nanowire is given by $\mathcal{H}_{\rm NW} = (p_x^2/2m^* - \mu_\gamma + eV_\gamma - \sigma_y\lambda p_x/\hbar)\tau_z + V_Z\sigma_x$, where m^* represents the effective electron mass, μ_γ is the chemical potential, V_γ denotes the biased voltage in the γ region, λ describes spin-orbit coupling, and $p_x = -i\hbar\partial_x$ is the momentum operator. The magnetic field B induces a Zeeman splitting $V_Z = g_{\rm eff}\mu_B B/2$ with $g_{\rm eff}$ the effective g factor and μ_B the Bohr magneton. The Pauli matrices σ (τ) act on the spin (particle-hole) spaces and $\mathcal{H}_{\rm NW}$ is written in terms of the spinor $\Psi(x) = [\psi_\uparrow(x), \psi_\downarrow(x)]^T$ with $\psi_s(x)$ annihilating an electron of s spin at position x.

Generally, the long-range pairing potential $\Delta_\gamma(x, x')$ can take various forms depending on details and degree of complexity incorporated into the model. Here we assume that the pairing between two particles decays as a power-law function of their spatial distance [70,73]. With this specification, the tight-binding Hamiltonian of H_γ over an M-site chain reads

$$\begin{aligned}\mathcal{H}_\gamma = &\sum_{j=1}^{M}[(2t - \mu_\gamma + eV_\gamma)c_j^\dagger c_j + V_Z c_j^\dagger\sigma_x c_j] \\ &+ \sum_{j=1}^{M-1}(-t c_j^\dagger c_{j+1} - i\,t_\lambda c_j^\dagger\sigma_y c_{j+1} + \text{H.c.}) \\ &+ \sum_{j=1}^{M}\sum_{\ell=0}^{M-1}(e^{i\phi_\gamma}\Delta_\ell c_{j,\uparrow}^\dagger c_{j+\ell,\downarrow}^\dagger + \text{H.c.}).\end{aligned} \tag{4}$$

The length of superconducting region is $L_S = Ma$ with $a =$ 10 nm denoting the lattice spacing. The nearest-neighbor hopping and spin-orbit coupling are described by parameter $t = \hbar^2/2ma^2$ and $t_\lambda = \lambda/2a$ in the lattice model. The annihilation operator of s spin on site j is $c_{j,\sigma}$ and some spin indices have been suppressed for brevity. Here ϕ_γ represents the phase of superconducting order parameter in the γ region, while the spatial-dependent part of pairing in both left and right regions is specified by

$$\Delta_\ell = \frac{\Delta}{(\ell+1)^\alpha}, \tag{5}$$

where Δ is the onsite superconducting pairing potential and $\ell = |i - j|$ gives the spatial distance between sites i and j. This type of long-range pairing interactions can be seen as a generalization of its counterpart in the extended Kitaev model. By tuning the power-law exponent to the short-range limit ($\alpha \to \infty$), the standard model of the hybrid superconductor-semiconductor Majorana nanowire is restored [71,73].

The tight-binding Hamiltonian of the normal region takes the same form of $\mathcal{H}_\gamma$ in Eq. (4) except that its length is $L_N = Na$ and chemical potential is μ_N. The proximity-induced superconductivity and applied voltage in this region are set to zero. The tunneling Hamiltonian in this lattice model reads

$$\mathcal{H}_T = \sum_s t_L d_{1,s}^\dagger c_{M,s} + t_R d_{N,s}^\dagger c'_{1,s} + \text{H.c.}, \tag{6}$$

with $d_{j,s}$, $c_{j,s}$, and $c'_{j,s}$ represent the annihilation operators in the central normal, left superconducting, and right superconducting region, respectively. $t_{L(R)}$ describes the tunneling coupling across the left (right) junction interface.

A. Phase diagram of the long-range superconducting nanowire

First, we discuss the phase diagram of the long-range superconducting region described by H_γ in Eq. (4). In the equilibrium case where $V_\gamma = 0$, the real-space Hamiltonian H_γ can be transformed into the Hamiltonian in momentum space as

$$\mathcal{H}(k) = (\varepsilon - 2t\cos k - 2\sigma_y t_\lambda \sin k)\tau_z + V_Z\sigma_x + \Delta(k)\tau_x \tag{7}$$

with Nambu spinor $[c_{k\uparrow}, c_{k\downarrow}, c_{-k\downarrow}^\dagger, -c_{-k\uparrow}^\dagger]^T$ and onsite energy $\varepsilon = 2t - \mu$. The long-range pairing terms of Eq. (5) in the momentum space reads

$$\Delta(k) = \Delta\left[1 + \sum_{\ell=1}^{\infty}\frac{2\cos k\ell}{(\ell+1)^\alpha}\right], \tag{8}$$

which is strictly convergent when $\alpha > 1$. In this case, one can verify that the long-range superconducting region modeled by Eq. (7) belongs to class BDI characterized by a $\mathbb{Z}$ invariant [73–75]. The corresponding topological invariant is given explicitly by [70]

$$W = \frac{1}{2}[\text{sgn}Z(\pi) - \text{sgn}Z(0)], \tag{9}$$

where $Z(k) = [\Delta(k) + 2i\,t_\lambda \sin k]^2 + (2t\cos k - \varepsilon)^2 - V_Z^2$. However, Eq. (9) is not applicable for $\alpha \leqslant 1$ since $\Delta(k)$ becomes divergent at $k = 0$ and the sign of $Z(0)$ is thus ill defined. Therefore, the contribution to topological invariant can only come from $Z(\pi)$. The relevant noninteger winding numbers can be defined as [73,76]

$$W = \begin{cases} -\frac{1}{2} & \text{for } |2t + \varepsilon| < \sqrt{V_Z^2 - \Delta^2(\pi)}, \\ +\frac{1}{2} & \text{for } |2t + \varepsilon| > \sqrt{V_Z^2 - \Delta^2(\pi)}, \end{cases} \tag{10}$$

by linearizing $Z(k)$ around the $k = \pi$ point. Detailed derivations are given in Appendix.

The corresponding phase diagram on the $\varepsilon - \alpha$ parameter plane are presented in Fig. 2(a). For the short-range regime with a large long-range exponent $\alpha \gg 1$, two topological branches bounded in $|2t - \varepsilon| < \sqrt{V_Z^2 - \Delta(0)^2}$ and $|2t + \varepsilon| < \sqrt{V_Z^2 - \Delta(\pi)^2}$ are symmetrically distributed about $\varepsilon = 0$. They correspond to a pair of opposite integer winding numbers $W = 1$ and $W = -1$, respectively. The energy spectra in these two branches are topologically equivalent to that of a standard Majorana nanowire and the system can host two unpaired MBSs at the ends of an open chain. The symmetry of these two short-range topological phases under $\varepsilon \to -\varepsilon$ is broken when the long-range pairings arise. We can identify that the topological region corresponding to $W = 1$ vanishes when α approaches the critical line $\alpha = 1$, while the phase associated with $W = -1$ exhibits no apparent deformations. Since the topological condition $V_Z > \sqrt{\mu^2 + \Delta^2(k)}$ holds at $k = 0$ [3], the critical long-range pairing exponent α_c satisfies the following relation:

$$\sqrt{V_Z^2 - \mu^2} = \Delta\left[1 + 2\sum_{\ell=1}^{L_S}(\ell+1)^{-\alpha_c}\right], \tag{11}$$

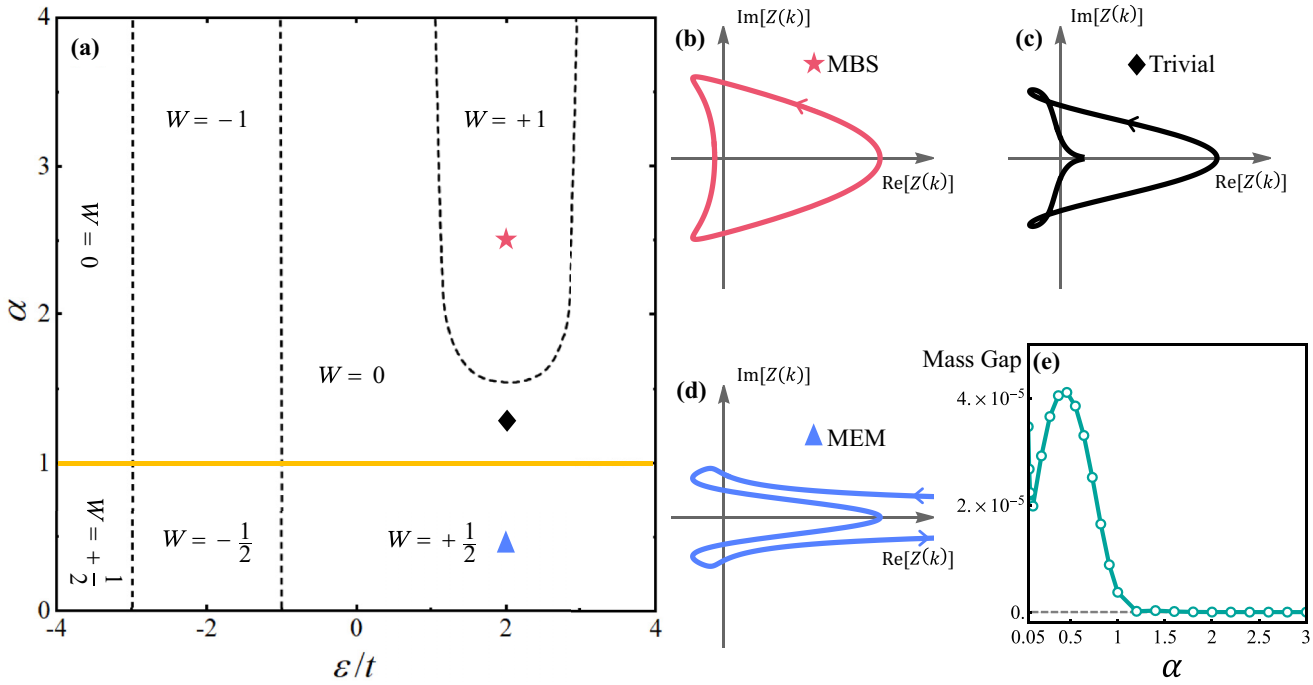

FIG. 2. (a) Phase diagram on the $\varepsilon - \alpha$ plane of a single long-range nanowire with power-law decaying pairing exhibits a dependence on the on-site pairing potential. [(b)–(d)] Trajectories of the winding vector on the complex plane at $\varepsilon = 2t$ for (b) MBSs in the topological short-range regime, (c) trivial states in the nontopological short-range regime, and (d) MEMs in the long-range regime. (e) Mass gap as a function of α in the long-range superconducting region with open boundary condition and $L_S = 1000a$. The other parameters are taken as $V_Z = t_\lambda = t$ and $\Delta = t/4$.

from which the topological transition points in the short-range regime can be extracted. For the strict long-range regime of $\alpha \leqslant 1$, the long-range pairing term $\Delta(k = 0)$ becomes divergent in the thermodynamic limit $L_S \to \infty$. The system is driven into two novel phases, corresponding to a pair of half-integer winding numbers $W = \pm 1/2$. The two critical lines traced by $\varepsilon = -2t \pm \sqrt{V_Z^2 - \Delta(\pi)^2}$ remain gapped in the long-range regime and become the boundaries that separate the $W = -1/2$ and the $W = 1/2$ sectors. The system can host nonlocal MEMs at the two wire ends in these long-range phases labeled by half-integer invariants.

We show the correspondence between bound states and the topological invariants by plotting the trajectory of winding vector $Z(k)$ in Figs. 2(b)–2(d). For the MBSs represented by the red star in the short-range regime of Fig. 2(a), the winding vector winds a completely closed contour around the origin in Fig. 2(b), producing an integer winding number $W = 1$. As illustrated in Fig. 2(c), the winding vector of a trivial nanowire in the short-range sector also traces a similar closed contour except that it excludes the origin, which results in zero winding number $W = 0$. However, for the long-range phase featured by MEMs, the divergent $Z(k)$ at $k = 0$ leaves the trajectory traced by the winding vector discontinuous on the real axis, which explains the half-integer winding number $W = 1/2$.

To further explore the different behaviors between the nonlocalities of MEMs and MBSs, we present mass gap of the lowest-energy eigenstates as a function of α in Fig. 2(e). First, we rewrite the tight-binding Hamiltonian given by Eq. (4) into the diagonal form $H_\gamma = \sum_{m=1}^{M} \xi_m \eta_m^\dagger \eta_m$. After the eigenvalues ξ_m are calculated, the mass gap η of an M-site open chain can be easily obtained as $\eta(M) = \min\xi_m$. Here we consider a quite long nanowire with $L_S = 1000a$. The mass gap of the subgap modes for $\alpha \geqslant 1$ is exponentially suppressed, which is an intrinsic feature of the MBSs in the topological short-range phase. In contrast, the finite mass gap η exhibits a algebraic dependence on α within the long-range phases, indicating a more slowly attenuated wave function overlap against the wire length between MEMs [38]. Note that we exclude the data around $\alpha = 0$ for visualization since the mass gap becomes divergent as the long-range pairings do not decay any more when α approaches zero.

B. Derivation of dc and ac Josephson currents

We now outline the formalism to calculate the Josephson currents in both equilibrium and nonequilibrium junctions. In an equilibrium Josephson junction with zero biased voltage $V = 0$, the corresponding phase-dependent supercurrents can be obtained from the following equation [77]

$$I(\phi) = \frac{2e}{\hbar}\frac{d\Omega}{d\phi}, \tag{12}$$

where Ω is a thermodynamic potential of the system dependent on the superconducting phase difference ϕ across the junction. The factor of 2 accounts for the Cooper pair charge and all the degeneracies are included in the potential Ω. This formula is valid for the general model of Josephson junction. In the following sections, we mainly focus on weak-linked junctions where the energy levels from the continuous spectrum contribute negligibly to the supercurrents [78]. Here we

choose Ω to be the grand potential of the superconductor, and the Eq. (12) can then be written as [77]

$$I_{dc}(\phi) = -\frac{2e}{\hbar}\sum_{p}\tanh\left(\frac{\xi_p}{2k_BT}\right)\frac{d\xi_p}{d\phi}, \tag{13}$$

where k_B is the Boltzmann constant, T is the temperature, and the summation is performed over all the discrete levels ξ_p in the superconducting gap. Hence the dc current-phase relation (CPR) of the finite-sized system modeled by Eqs. (4) and (6) at zero temperature can be further simplified to

$$I_{dc}(\phi) = -\frac{e}{\hbar}\sum_{n>0}\frac{dE_n}{d\phi}, \tag{14}$$

where $E_{n>0}$ can be explicitly obtained as the nth positive eigenenergy by diagonalizing the total Hamiltonian in Eq. (1). Here the summation over spin degree is explicitly assumed since the spin degeneracy is lifted by the Zeeman field V_Z, which results in the drop of factor 2 for spin degeneracy in Eq. (14) [79]. Another experimentally relevant transport property is the critical current $I_c = \max_\phi I(\phi)$, which is defined as the maximum supercurrent supported by the junction with the phase difference ϕ varying.

For the nonequilibrium Josephson junctions, we adopt a partition-free approach where the superconducting regions are assumed coupled in equilibrium to the normal region before applying the biased voltage [80]. As we switch on the bias voltage V after $t \geqslant 0$, the only time-dependent component of the nonequilibrium total Hamiltonian $H(t)$ are the proximity-induced superconducting pairing terms and in the lattice model it can be written as

$$\mathcal{H}^{\gamma}_{\rm SC}(t) = \sum_{j=1}^{M}\sum_{\ell=0}^{M-1} e^{i(\phi_\gamma+2eV_\gamma t)}\Delta_\ell c^\dagger_{j,\uparrow}c^\dagger_{j+\ell,\downarrow} + \text{H.c.}, \tag{15}$$

where we define $\phi_\gamma(t) \equiv \phi_\gamma + 2eV_\gamma t$ as the evolution of the superconducting phase in the γ region. We denote $\mathbf{H}(t)$ the matrix form of the time-dependent Hamiltonian $H(t \geqslant 0)$ in the tight-binding basis. Here $H(t=0)$ describes the equilibrium Hamiltonian H in Eq. (4). In the Bogoliubov–de Gennes space, the generic component of $\mathbf{H}(t)$ is a block matrix

$$\mathbf{H}_{\nu\nu'}(t) = \begin{bmatrix} h_{\nu\nu'}(t) & \vartheta_{\nu\nu'}(t) \\ \vartheta^\dagger_{\nu\nu'}(t) & -h_{\nu\nu'}(t)\end{bmatrix}, \tag{16}$$

where $\nu = 1,\ldots,2M+N$ labels the sites of the whole system and $h(t)$, $\vartheta(t)$ represent the nanowire and superconducting components of Hamiltonian in the subspace.

The time-dependent supercurrent across the left junction interface can be calculated via the nonequilibrium Green's function method [78]

$$I_{ac}(t) = 2\sum_m t_L \text{Re}\,\text{Tr}[\mathbf{G}^<_{1m}(t,t)], \tag{17}$$

where subscript 1 labels the left most site in the normal region and m label the states in the left superconducting region. The supercurrent flowing through the right junction can be defined in an analogous way with Eq. (17). The time-dependent lesser Green's function $\mathbf{G}^<(t,t')$ takes the following form [81]:

$$\mathbf{G}^<(t,t') = i\sum_q f(E_q)\begin{bmatrix} u_q(t)u_q^\dagger(t') & u_q(t)v_q^\dagger(t') \\ v_q(t)u_q^\dagger(t') & v_q(t)v_q^\dagger(t')\end{bmatrix}. \tag{18}$$

Here $f(E) = 1/[1+\exp(E/k_BT)]$ is the Fermi-Dirac distribution. The qth eigenenergy and eigenstate of time-dependent Hamiltonian $H(t)$ are denoted by E_q and a two-component vector $\Phi_q(t) = [u_q(t), v_q(t)]^T$ in the Nambu space.

Following the partition-free method, we first calculate the initial lesser Green's function $\mathbf{G}^<(0,0)$, which is related to the equilibrium Hamiltonian $\mathbf{H}(0)$ as [81]

$$\mathbf{G}^<(0,0) = \frac{i}{1+\exp[\mathbf{H}(0)/k_BT]}, \tag{19}$$

which in the tight-binding basis takes the following form:

$$\mathbf{G}^<_{\nu\nu'}(0,0) = i\sum_q f(E_q)\begin{bmatrix} u_q(\nu)u_q^\dagger(\nu') & u_q(\nu)v_q^\dagger(\nu') \\ v_q(\nu)u_q^\dagger(\nu') & v_q(\nu)v_q^\dagger(\nu')\end{bmatrix}. \tag{20}$$

where $u_q(\nu)$ and $v_q(\nu)$ give the particle and hole wave functions on site ν. They are specified by solving the secular equations for the static eigenstates Φ_q,

$$\sum_{\nu'}\mathbf{H}_{\nu\nu'}(0)\Phi_q(\nu') = E_q\Phi_q(\nu). \tag{21}$$

The time evolution of eigenstates are governed by the time-dependent Bogoliubov–de Gennes equations, which can be expressed in the compact form

$$i\dot{\Phi}_q(\nu,t) = \sum_{\nu'}\mathbf{H}_{\nu\nu'}(t)\Phi_q(\nu',t). \tag{22}$$

Here the solutions of Eq. (22) are given by

$$\Phi_q(\nu,t) = \sum_{\nu'}\mathbf{U}_{\nu\nu'}(t,0)\Phi_q(\nu',0) \tag{23}$$

with the initial condition $\Phi_q(\nu,0) = \Phi_q(\nu)$ and the time evolution operator $\mathbf{U}(t,0)$ is defined as

$$\mathbf{U}(t,0) = T\exp\left[-i\int_0^t dt'\mathbf{H}(t')\right], \tag{24}$$

where T represents the time-ordering operator. The lesser Green's function is propagated in time as [78]

$$\mathbf{G}^<(t,t) = \mathbf{U}(t,0)\mathbf{G}^<(0,0)\mathbf{U}^\dagger(t,0). \tag{25}$$

Since the bias voltage is constant in time, we can discretize the time into a sequence $t_n = n\delta t$ with n a positive integer. The evolution of the lesser Green's function can then be numerically solved via a time-stepping procedure

$$\mathbf{G}^<(t_n,t_n) = \widetilde{\mathbf{U}}_n\mathbf{G}^<(t_{n-1},t_{n-1})\widetilde{\mathbf{U}}_n^\dagger, \tag{26}$$

where the discretized time evolution operator $\widetilde{\mathbf{U}}_n = \exp[-i\delta t\mathbf{H}(t_n)]$ propagates the lesser Green's function from t_{n-1} to t_n. Inserting this numeric result back to Eq. (17), we can then obtain the ac Josephson supercurrents.

III. RESULTS

A. The current-phase relation of LRK-based Josephson junctions

To demonstrate the effects of long-range pairing on the Josephson supercurrents, we will first study a simpler model where the junction are composed of two weakly connected long-range Kitaev chains (LRK). Here we consider a generalization of standard Kitaev chain in the presence of long-range pairings decaying algebraically as a power-law function of site distance, and nonlocal hopping terms are not taken into account. The corresponding long-range Hamiltonian over an N-site chain reads [50]

$$H_{\mathrm{LRK}} = -\mu \sum_{j=1}^{N} c_j^\dagger c_j - t \sum_{j=1}^{N-1} c_j^\dagger c_{j+1} + \mathrm{H.c.} + \Delta \sum_{j=1}^{N} \sum_{\ell=1}^{N-1} \ell^{-\alpha} c_j c_{j+\ell} + \mathrm{H.c.}, \tag{27}$$

where ℓ denotes the distance between different sites. The standard Kitaev Hamiltonian, which involves only nearest-neighboring pairings, is recovered in the short-range limit $\alpha \to \infty$.

The long-range Kitaev models proposed by previous literature can be exactly solved within the standard approach to noninteracting fermion problems [38], allowing us to give its phase diagram in the $\mu - \alpha$ plane with closed boundary condition. As displayed in Fig. 3(a), we can identify a simpler diagram in comparison to Fig. 2(a). When $\alpha < 1$, two novel phases have been found out and the corresponding winding number W takes the values $W \pm 1/2$ (at $\mu \gtrless 1$). They are not continuously connected to the short-range phases in $\alpha > 1$, which labeled by integer winding numbers $W = 0, 1$, for trivial states and topological MBSs, respectively. The long-range phases within $\alpha < 1$ and $\mu < 1$ are suggested to support a pair of topological MEMs localized at the two ends of Kitaev chain, which can be attributed to the divergencies in the quasiparticle spectrum.

We then consider a Josephson junction consists of two weak-linked LRK described above and extract its CPR in the equilibrium configuration. First, we investigate the edge modes in the phase at $\alpha > 1$ and $|\mu| < 1$, labeled by the red star in Fig. 3(a). In the case, the structure of these edge modes is qualitatively equivalent to those in the nontrivial Kitaev chain: Two real fermionic modes emerge, with wave functions localized at the endpoints of the chain, which eventually evolve into the MBSs with vanishing mass in the infinite-chain limit. Figure 3(b) depicts a steep sawtooth CPR profile at the phase difference $\phi = \pi$ induced by this short-range subgap mode. This means that a parity-protected zero crossing is allowed by MBSs, which prevents the system evolving adiabatically back to the ground state after the superconducting phase rotates over 2π radians. This indicates that both the inner and outer pairs of edge modes exhibit clear MBSs characteristics at the two junction interfaces. For $\alpha < 1$, there are still subgap modes with wave functions mostly localized around the endpoints of the chain, which can be identified as a remnant of the edge modes in the phase at $\alpha > 1$ and $|\mu| < 1$. However, the wave function overlap of long-range subgap modes will keep finite even in the thermodynamic limit, thus dubbed as MEMs. The CPR also manifests itself differently in this long-range regime. As shown in Fig. 3(c), I_{dc} instead exhibits a smooth sinelike curve, implying the absence of zero crossing within the whole $0 \leqslant \phi \leqslant 2\pi$ interval in the MEMs-dictated phase.

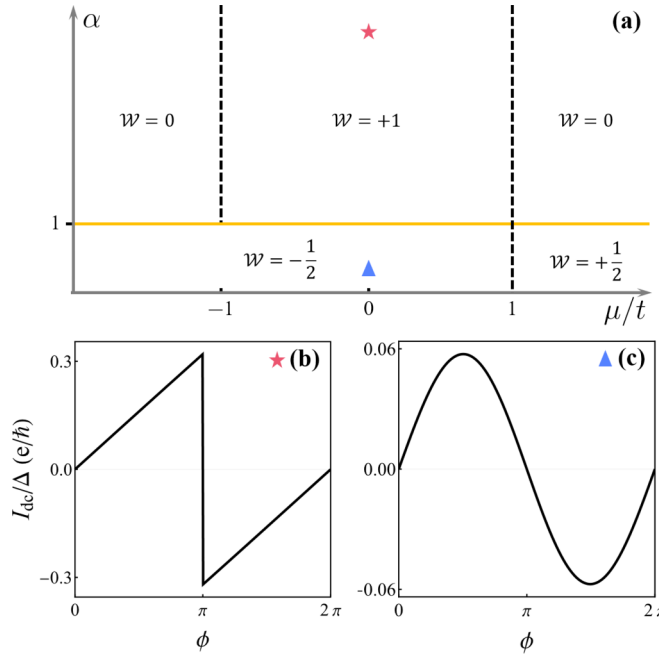

FIG. 3. (a) Phase diagram in the $\mu - \alpha$ plane of a long-range Kitaev chain with its pairing interactions quantified by power-law decay rate α, adapted from Ref. [52]. The winding number $W = 0$, $W = 1$ are associated with the trivial and topological phases in the short-range sector ($\alpha > 1$), while $W = +1/2$, $W = -1/2$ corresponds to the unconventional trivial and topological phases in the long-range sector ($\alpha < 1$). [(b) and (c)] Phase-dependent dc Josephson currents of a LRK-based Josephson junction involving (b) MBSs in the short-range sector ($\alpha \gg 1$), or (c) MEMs in the long-range sector ($\alpha = 0.25$). The chemical potentials are fix at $\mu = 0$.

B. dc Josephson effects

We now discuss the effects of long-range pairing on the Josephson current in a realistic nanowire-based Josephson junction. Let us start with the low-lying energy spectra of the device. In Figs. 4(a) and 4(b), we present the Zeeman-dependent low-energy spectrum at $\phi = \pi$ for short-range ($\alpha = 10$) and long-range phases ($\alpha = 0.2$), respectively. In the short-range case ($\alpha = 10$), the superconducting spectrum shown in Fig. 4(a) undergoes a topological phase transition at $V_Z = V_{ZC} \equiv \sqrt{\mu_S^2 + \Delta^2}$ (vertical gray dashed line) and a gap closing is anticipated at this point. In the topological phase, the four lowest levels of edge modes appear almost pinned to zero energy with an increasing V_Z, which corresponds to the four unpaired MBSs located at the outer inner ends of the Josephson junction. However, the situation is different in the long-range regime. Figure 4(b) demonstrates that the splitting oscillations of edge modes spectra persists in the topologically nontrivial region $V_Z > V_{ZC}$ accompanied by sporadic zero crossings.

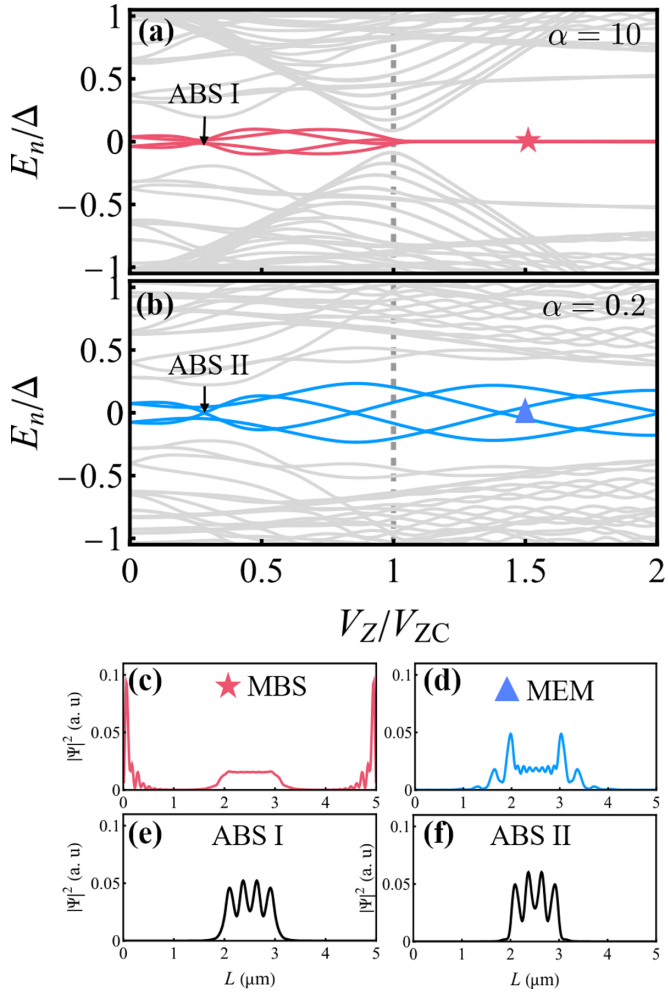

FIG. 4. [(a) and (b)] Low-lying eigenenergies in a long tunneling junction as a function of Zeeman field V_z in the (a) short-range regime $\alpha = 10$ and (b) long-range regime $\alpha = 0.2$. [(c) and (d)] Spatial distributions of the wave functions for the lowest four eigenstates in the short-range regime marked in (a) by the red star and black annotation. [(e) and (f)] The same quantities while in long-range regime indicated in (b) by the blue triangle and black annotation. The other parameters are taken as $\mu_S = \Delta = 0.5\,\text{meV}$, $t = 50\Delta$, and $t_\lambda = 4\Delta$. The chemical potential in the normal region is set as $\mu_N = \mu_S/2$ to induce zero-energy ABSs via the confinement effect [82].

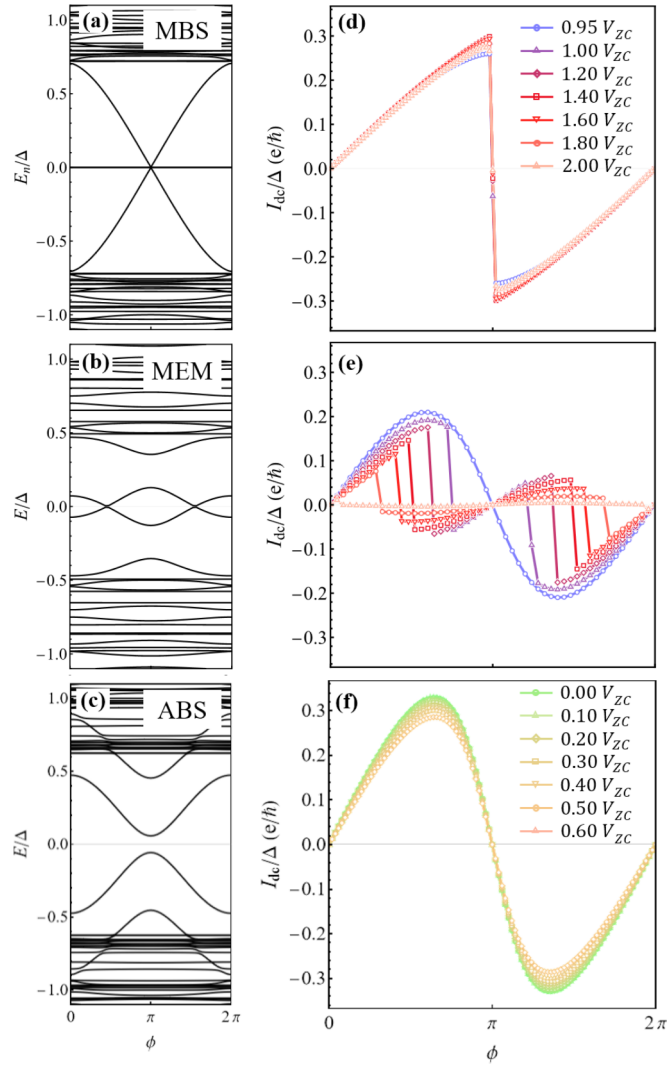

FIG. 5. [(a) and (c)] Phase-dependent low-lying eigenenergies in the (a) short-range $\alpha = 10$, (b) long-range regime $\alpha = 0.2$ at $V_Z = 1.5V_{ZC}$, and (c) a nontopological case at $V_Z = 0.5V_{ZC}$, $\alpha = 10$ for comparison. [(d) and (f)] Phase-dependent dc Josephson currents for different V_Z in the (d) short-range $\alpha = 10$, (e) long-range regime $\alpha = 0.2$, and (f) nontopological cases with $V_Z \leqslant 0.6V_{ZC}$, $\alpha = 10$ accompanied by ABSs.

These behaviors can be further illustrated by looking at the total wave function of the four lowest states in Figs. 4(c) and 4(d). In the topological phase at $V_Z = 1.5V_{ZC}$, the four lowest levels shown in Fig. 4(c) represent four MBSs (red solid curves). We note that the outer MBSs wave functions exhibit an exponentially suppression, which results in negligible zero-energy splitting as V_Z increases. For the inner MBSs, the spatial overlap is considerably enhanced across the normal region. In contrast, for the long-range regime shown in Fig. 4(d), MEMs (blued solid curves) are always mainly located at the junction interfaces and do not induce a spatial distribution at the outer ends of the system. Additionally, we also calculate the spatial distributions of ABSs in both short-range and long-range sectors. As illustrated by Figs. 4(e) and 4(f), both ABSs exhibit a diffusive wave function largely entering into the central normal region.

Figure 5 demonstrates the dc Josephson currents induced by three types of subgap modes. In order to highlight their different localization natures, we consider a short-junction scenario ($L_N \ll \xi$) with high transparency $t_L = t_R = t$. First, we give the phase-dependent low-lying spectra of MBSs, MEMs, and ABSs in the long-range regime, respectively, in Figs. 5(a)–5(c). For all three cases, we observe dense energy spectra emerging as the quasicontinuum above the gap which are almost dispersionless within the whole 2π period of ϕ. In the MBSs-dictated phase illustrated by Fig. 5(a), we notice that the lowest two energy levels, associated to the outer MBSs, are insensitive to remaining at zero energy, whereas the inner MBSs are submerged with the quasicontinuum at $\phi = 0, 2\pi$. Although its energy levels gradually detach from the continuum as the phase difference deviates from 0 or 2π, it only touch zero at $\phi = \pi$, indicating that the short-range end states can only manifest MBSs characteristics at this single

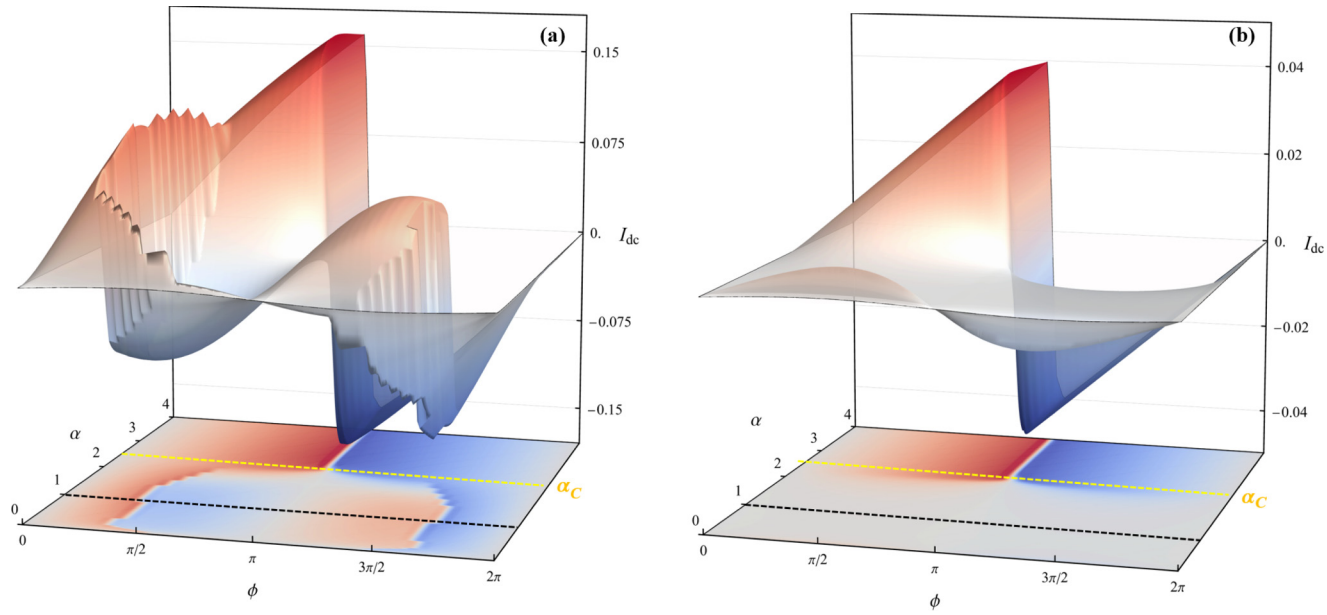

FIG. 6. [(a) and (b)] Phase-dependent dc Josephson current I_{dc} on the $\alpha - \phi$ plane at $V_Z = 1.5V_{ZC}$ in the (a) short junction case with $L_N = 10a$ and (b) long junction case with $L_N = 100a$. Other parameters are taken the same as in Fig. 5.

point. Moreover, the energy splitting at $\phi = \pi$ is considerably reduced, even vanished.

On the contrary, the long-range spectra characterized by MEMs in Fig. 5(b) shows different subgap behaviors. Notice that the two lowest levels associated with the MEMs located at junction interfaces are not pinned at zero energy. Instead, they only exhibit linear dispersion at two crossing points symmetrically deviating from $\phi = \pi$. The next two lowest levels stay closer to the quasicontinuum and acquire no zero crossings throughout the whole 2π period of ϕ, implying the negligible wave functions located at outer ends of the system and the strong overlap between MEMs. As a comparison, the energy-phase relation of ABSs demonstrates a smoother behavior near the zero energy and there is no zero crossing in its low-lying energy spectra throughout the whole 2π period of ϕ.

The phase-dependent dc supercurrents I_{dc} in the same short-junction scenario are presented in Figs. 5(c) and 5(d) for different values of the Zeeman field V_Z in the short-range and long-range regimes, respectively. In the case of short-range phase, Fig. 5(d) depicts a steep sawtooth CPR profile at $\phi = \pi$, signaling an MBS-induced protected crossing at this point. We also note how the overall CPR shape and the critical supercurrent I_c in the strong short-range regime remains almost unaltered by the Zeeman field V_Z. The CPR exhibits different behaviors in a strong long-range regime $\alpha = 0.2$. As shown in Fig. 5(d), the emerging MEMs give rise to a distinct CPR which develops a zigzag profile involving two sign-reversal points symmetrically located before and after $\phi = \pi$, indicating a 0-π transition in the supercurrent [83]. This transition arises from the zero-energy crossings in the low-energy spectrum, as depicted in Fig. 5(b). The zero crossings permitted by MEMs anticipate a shift from $\phi = \pi$ toward $\phi = 0$ as V_Z increases. For $V_Z < V_{ZC}$, the trivial ABSs could be generated and I_{dc} exhibits a sinelike behavior, as illustrated in Fig. 5(f).

In addition, we also give the CPR as a function of long-range pairing exponent α in Fig. 6. Since the low-lying spectra of the subgap bound states sensitively depend on the length of the normal region, we consider both the short and long junction scenarios. For a short Josephson junction case shown in Fig. 6(a), following similar analyses from the previous discussion, the system is driven into a long-range phase with MEMs when $\alpha < 1$. Compared with the exponentially suppressed wave functions of MBSs, the leakage of MEMs into the central normal region exhibits a much slower algebraic decay, leading to a more prominent energy hybridization. Consequently, the zero crossings of its low-lying spectra no longer degenerate at a single point, which results in two sign-reversal points away from $\phi = \pi$. In the short-range phase of $1 < \alpha < \alpha_c$, the sign reversal of the Josephson current moves to the point of $\phi = \pi$ gradually. With the further increase of α and for $\alpha > \alpha_c$, the system is driven into the topological superconducting phase and a pair of MBSs is induced, manifesting a sharp sign reversal at the point $\phi = \pi$ in the current-phase relation.

Figure 6(b) demonstrates the effect of long-range pairing on the Josephson current as a function of the phase difference ϕ in the long junction case, where we take $L_N = 100a$. In this case, the smoother wave function overlaps across the central normal region makes the subgap bound states less related to ϕ. In the long-range phase, the longer junction produce a more flat low-lying spectrum of MEMs near the zero energy. Correspondingly, a much smoother current phase relation is induced over $0 \leqslant \phi \leqslant 2\pi$, as plot in Fig. 6(b). Meanwhile, the critical currents related to MEMs are significantly suppressed for the long junction case. However, in the short-range phase hosting MBSs, the parity-protected exact zero crossing still holds and the sign reversal of the Josephson current still appears at $\phi = \pi$.

The critical supercurrents as a function of the Zeeman splitting are plotted in Fig. 7 for the short and long

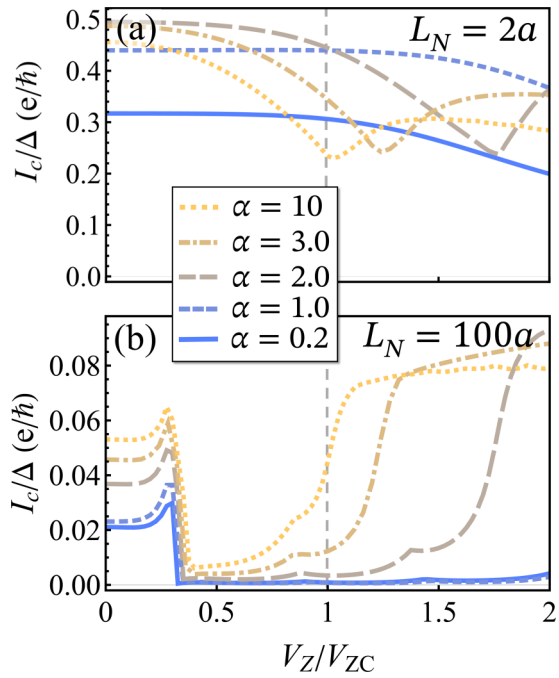

FIG. 7. Critical current I_c as a function of the Zeeman splitting V_Z with the long-range exponent taking values in $0.2 \leqslant \alpha \leqslant 10$ for (a) the short junction case with $L_N = 2a$ and (b) long junction case with $L_N = 100a$. The rest of parameters are the same as in Fig. 5.

junction cases, respectively. We first consider the short junction case $L_N = 2a$, compared to the Majorana coherence length $\xi \sim 50a$. In the short-range cases $\alpha > 1$, the critical currents indicate a nonmonotonic dependence on the Zeeman field V_Z. The minimum values of I_c gradually reach $V_Z = V_{ZC}$ since the contributions of long-range pairing term to the spectrum decay rapidly as α approaches 1. When the device experiences the phase transition, the appearance of MBSs dominates the contributions to the supercurrents and its unique nonlocality is helpful to enhance the Josephson current. Differently, for the long-range case $\alpha \leqslant 1$, the critical current slightly decreases and exhibits a smoother behavior with the increase of V_Z. This implies that MEMs and ABSs produce similar contributions to the dc Josephson currents.

It is illustrated in Fig. 7(b) for the long junction case $L_N = 100a \sim 2\xi$. In the region of $V_Z < V_{ZC}$, the critical currents for both the short-range and long-range cases exhibit similar behaviors and undergo a large decline at $V_Z \sim \mu_N$, which is due to the emergence of near-zero energy ABSs. As V_Z further increases, the critical current I_c in the short-range phase is continuously enhanced until its value reaches a plateau. In contrast, the critical current I_c in the long-range phase remains significantly suppressed. The different field-dependent I_c behaviors between the short-range and long-range phases are the consequences of nonlocal natures of MBSs and MEMs. In the topological short-range phase, the overlap of the well-localized inner MBSs is exponentially suppressed, leading to a protected zero crossing at the phase difference $\phi = \pi$ in the energy spectrum. The current-phase relation is almost unaffected with the increase of V_Z. While for the long-range phase, the MEMs-induced crossings are notably smeared out since the wave function of MEMs is only algebraically suppressed against the increasing L_N. In this case, the energy splitting of MEMs is less sensitive to the Zeeman field for longer L_N, and the critical current I_c is thus suppressed.

C. ac Josephson effects

For the equilibrium case, a given phase difference ϕ is maintained for an infinitely long time, so the occupation numbers of the subgap states have enough time to relax to thermodynamic equilibrium. We now study the case where the Josephson current tunneling across a junction biased by a small voltage V. This bias makes the phase difference take time dependent form $\phi(t) = \phi_0 + 2eVt/\hbar$ and the state of the system is determined dynamically starting from the initial conditions, where the initial phase difference $\phi_0 = \pi$ is taken for $t = 0$. In the long time limit, a finitely dissipative Josephson junction would exhibit an exact 2π-periodic ac supercurrent. As a result, few signatures remain to qualitatively distinguish the CPR profiles associated with different edge modes if system has reached the thermodynamic equilibrium. However, topologically protected edge modes exhibit crucial differences in their spectra that lead to diverse supercurrent behaviors in the transient regimes [30]. To further explore these features, we extract the ac current-phase relation from Eq. (17) in Figs. 8 and 9 with different values of V_Z and α for the first few 2π periods in a short-junction limit with $L_N = 2a$.

The properties of the ac Josephson current can be divided into two distinct regimes in respect of the biased voltage V and Majorana hybridization energy δ_M. First, the adiabatic region is identified when $V \ll \delta_M$. In this regime, the Josephson current is approximately 2π periodic since the applied voltage cannot support the Landau-Zener transition. When we tune up the voltage to $V = 2\delta_M$, the voltage is high enough to support the Landau-Zener transition. Figure 8(a) shows the contour plot for ac Josephson current as a function of the Zeeman field V_Z and time period with a fixed bias voltage $V = 2\delta_M$. Here we fixed $\alpha = 10$ in the short-range regime. One can identify that the 2π periodicity is quite stable when the system stays in the topologically trivial phase $V_Z < V_{ZC}$. As we increase V_Z to drive the system into topological phase, the stability of the 2π periodic current decays rapidly and begin to develop a quasi-4π periodicity. This 4π periodicity become more consolidation as the Zeeman field further increases. The 4π Josephson current can be sustained for a significant amount of time in these topological sectors. On the contrary, within the long-range regime, the period is always 2π as shown in Fig. 8(b), exhibiting a stable periodicity against various V_Z values across both the topologically trivial and nontrivial phases. This enhanced higher-order Josephson current is caused by the strong hybridization of bound states localized at the normal-superconductor interfaces. It can be attributed to trivial ABSs in the $V_Z > V_{ZC}$ phase and MEMs when $V_Z < V_{ZC}$. The different periodicity stabilities against a varying Zeeman field can be used to distinguish whether the system lies in short-range or long-range phase.

The dependence of the ac Josephson currents on different α is further demonstrated in Fig. 9. When the long-range pairings decay fast in the superconducting regions, as shown in Fig. 9(a) with $\alpha = 10$, the fractional Josephson effect

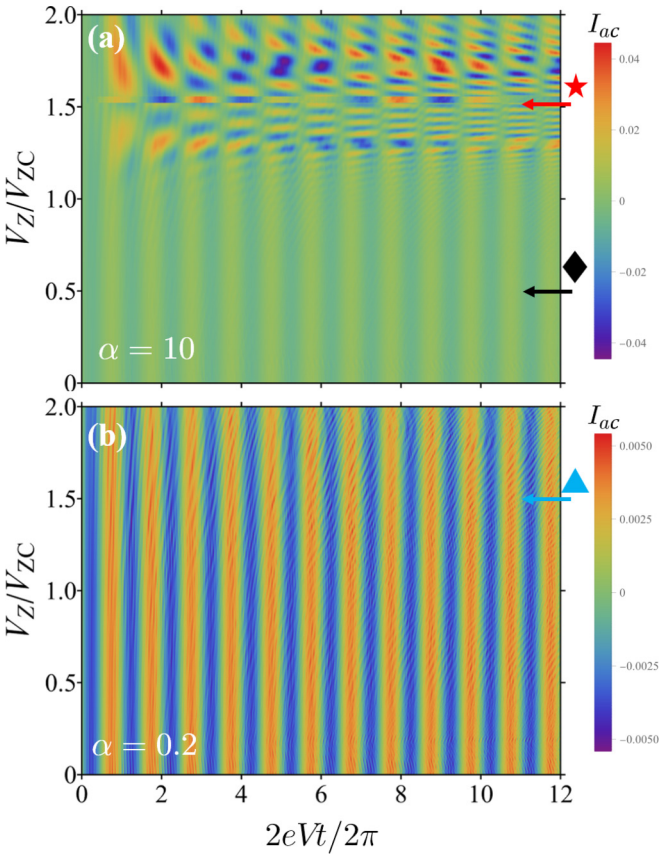

FIG. 8. (a) Time-dependent ac Josephson currents as a function of phase difference ϕ and Zeeman field V_Z in the short-range regime $\alpha = 10$. (b) The same quantity but in the long-range regime $\alpha = 0.2$. Color symbols mark the cut-lines where the CPR are extracted accompanied by MBSs (red star), trivial states (black rhombus), and MEMs (blue triangle), respectively. The coherence length and wire length of the superconducting region are reduced to $\xi \sim t/\Delta = 5$ and $L_S = 20a$ to alleviate the computation of Eq. (26) in small time steps. Other parameters are the same as in Fig. 4.

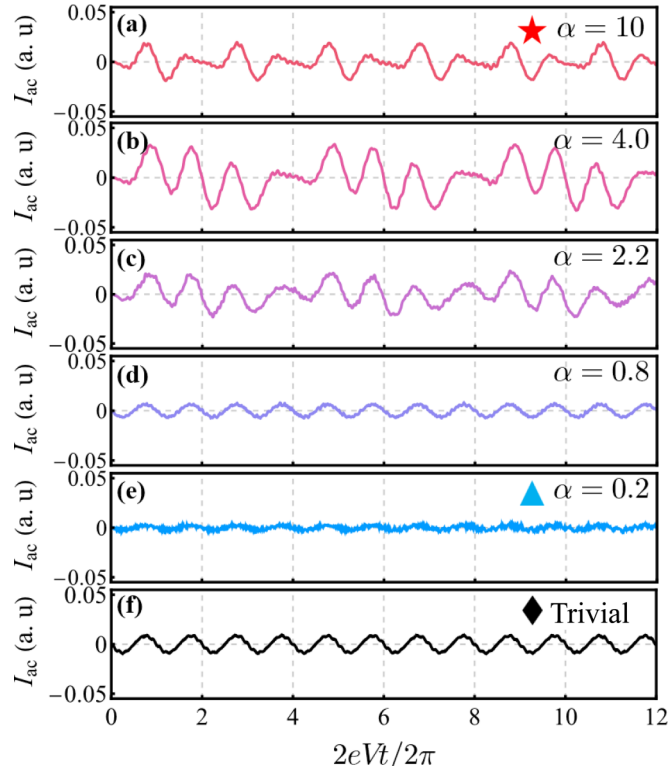

FIG. 9. [(a)–(e)] Time-dependent ac Josephson currents at $V = 2\delta_m$ over a wide range of long-range decay rates: (a) $\alpha = 10$ marked by the red star in Fig. 8(a), (b) $\alpha = 4.0$, (c) $\alpha = 2.2$, (d) $\alpha = 0.8$, and (e) $\alpha = 0.2$ marked by the blue triangle in Fig. 8(b). (f) Same current measurement marked by the black rhombus in Fig. 8(a) in the nontopological regime.

manifests as a 4π periodic current-phase relation with the MBSs-mediated tunneling process dominating the supercurrents, which differs from the adiabatic 2π supercurrent assisted by Cooper-pair hoppings. As α further decreases, ac Josephson currents plotted in Figs. 9(b) and 9(c) exhibit an expanded quasiperiodicity of 8π which doubles the period extracted from Fig. 9(a). The amplitude of critical supercurrents also sees an nonmonotonic modulation before the superconducting regions enter the long-range phases.

When $\alpha < 1$, the superconducting regions are driven into the MEMs-associated long-range phases and a 2π periodicity in ac Josephson currents is restored, as shown in Figs. 9(d) and 9(e). In the long-range phase hosting MEMs, only the two lowest-lying energy levels are detached from the quasicontinuum and the hybridization between the two levels destroy the parity-protected crossing at phase difference $\phi = \pi$. As a consequence, the 4π periodicity of the Josephson current does not appear any more, which is similar to the state evolution accompanied by trivial ABSs [30]. Therefore, the ac CPR can serve as an valid signature to distinguish the existence of MBSs and MEMs in the presence of a strong Zeeman field. Additional to the period reduction, Fig. 9(e) reveals that the critical supercurrents is considerably suppressed as α approaching the long-range limit, leading to a prominent fast oscillation in the CPR profile. This oscillatory pattern can be attributed to the divergence originates from the barely attenuated long-range pairing terms in the energy spectrum. As a result, the sinusoidal behavior of as Josephson currents are almost smeared out by the fast oscillations in the long-range limit $\alpha \to 0$. Additionally, the trivial ABSs dominate the subgap modes during the supercurrents transport process in both short-range and long-range phases at low Zeeman fields. The ac Josephson currents with these nontopological origins also acquires a 2π periodicity on the time-dependent phase difference $\phi(t)$, as typically presented in Fig. 9(f) with $\alpha = 10$, $V_Z = 0.5V_{ZC}$. The ABSs-mediated nonequilibrium CPR resembles the ac supercurrents profile sustained in the adiabatic regimes where the applied bias voltage cannot support the Landau-Zener transition.

IV. CONCLUSION

In summary, we investigated the long-range Josephson junction where two superconducting regions with power-law decayed pairings are connected through a central normal region. In the short-junction scenario, the MBSs can induce a steep sawtooth current-phase relation at the phase difference

$\phi = \pi$, signaling a parity-protected zero crossing at this point that prevents the system evolving adiabatically back to the ground state after the superconducting phase rotates over 2π radians. While in the long-range regime hosting MEMs, the CPR instead develops a zigzag profile involving two sign-reversal points symmetrically located before and after $\phi = \pi$, indicating a 0-π transition in the supercurrent. The critical supercurrent induced by MEMs is significantly suppressed in a long Josephson junction, as opposed to the stable large value of the critical currents seen in the short-range regimes. As a comparison, the zero-energy ABSs can result in smooth CPR without any sign-reversal points.

We also discuss the ac Josephson currents under bias voltage with different values of Zeeman field and the power-law decaying rate. It is found that, in the short-range regime, the 2π periodicity of ac currents decays rapidly and develop a 4π periodicity as we tune up the Zeeman field to drive the system into topological phase. On the contrary, the CPR associated with MEMs exhibit a stable 2π-periodic current against a wide range of Zeeman field values. This feature of the Josephson current can serve as a valid probe to distinguish the short-range phase from the long-range phase.

Until now, the strict long-range phase at $\alpha < 1$ has not been realized, and it is a long way to finally implement the fine-tuning of long-range interactions. Nevertheless, the long-range couplings between the impurity states have been experimentally observed in a chain of magnetic impurities on two-dimensional superconductors [54–58]. Recently, the topological physics has been widely simulated by electric circuits [62–65] and photonic waveguide arrays [84–86], such as the edge states, high-order topology, and even the non-Abelian braidings. It is expected that the long-range phase and MEMs could be realized in chains of magnetic atoms on the surface of a superconductor or in electric circuits.

ACKNOWLEDGMENTS

This work was supported by the National Natural Science Foundation of China under Grants No. 12074209 and No. 12274063, the Fundamental Research Funds for the Central Universities (No. ZYGX2019J100) and the Open Project of State Key Laboratory of Low-Dimensional Quantum Physics (Grant No. KF202008).

APPENDIX: DERIVATION OF THE TOPOLOGICAL INVARIANTS FOR THE LONG-RANGE SUPERCONDUCTING NANOWIRES

In this section, we detail the derivations of topological invariants in Eq. (9) and Eq. (10) of the main text. The long-range superconducting region modeled by $\mathcal{H}(k)$ in Eq. (7) belongs to class BDI with a $\mathbb{Z}$ invariant and respects the particle-hole symmetry $\mathcal{C} = \tau_y\sigma_y\mathcal{K}$ [73–75] with $\mathcal{K}$ denoting the complex conjugation. Therefore, $\mathcal{H}(k)$ can be expressed as a block off-diagonal form after a unitary transformation

$$U\mathcal{H}(k)U^\dagger = \begin{bmatrix} 0 & \mathcal{Q}(k) \\ \mathcal{Q}(k)^\dagger & 0 \end{bmatrix} \tag{A1}$$

with the antidiagonal component

$$\mathcal{Q}(k) = [\Delta(k) + 2it_\lambda \sin k] - i(2t\cos k - \varepsilon)\sigma_y - V_Z\sigma_z. \tag{A2}$$

Then the Berry connection of the system can be written as [74]

$$A_k = \frac{1}{2i}\partial_k \ln(\det\mathcal{Q}). \tag{A3}$$

The corresponding winding number can then be calculated by counting the number of quantized Berry phases in terms of π over the first Brillouin zone [70,73,74]

$$W = \frac{1}{\pi}\oint dkA_k = \frac{1}{2\pi i}\oint dk\partial_k \ln Z(k). \tag{A4}$$

where $Z(k) \equiv \det[\mathcal{Q}(k)]$ takes the explicit form

$$Z(k) = [\Delta(k) + 2it_\lambda \sin k]^2 + (2t\cos k - \varepsilon)^2 - V_Z^2, \tag{A5}$$

which can also be expressed in the polar form as $Z(k) = |Z(k)|\exp[i\varphi(k)]$ with $\varphi(k) \equiv \arg Z(k)$. Consequently, the winding number computation is further simplified to

$$W = \frac{1}{2\pi i}\oint dk\partial_k[\ln|Z(k)| + i\varphi(k)] = \frac{1}{2\pi}\oint dk\partial_k\varphi(k), \tag{A6}$$

where the contribution of the first term vanishes under the closed integration due to the periodicity of $|Z(k)|$ in the first Brillouin zone. It is noted that the relation

$$-\varphi(k) = \varphi(-k) \mod 2\pi \tag{A7}$$

holds since $Z(k)$ respects the particle-hole symmetry $\mathcal{C}$. Inserting these results back into Eq. (A6), we can finally deduce the calculation of winding number to

$$\begin{aligned} W &= \frac{1}{2\pi}\left[\int_{-\pi}^{0} dk\partial_k\varphi(k) + \int_0^{\pi} dk\partial_k\varphi(k)\right] \\ &= \frac{1}{\pi}\int_0^{\pi} dk\partial_k\varphi(k) \\ &= \frac{1}{\pi}[\varphi(\pi) - \varphi(0)], \end{aligned} \tag{A8}$$

which coincides with the following form [70]:

$$W = \frac{1}{2}[\mathrm{sgn}Z(\pi) - \mathrm{sgn}Z(0)]. \tag{A9}$$

This is exactly the Eq. (9) in the main text.

However, Eq. (A9) is only legitimate when the superconducting region is in the short-range regime ($\alpha > 1$). In the strict long-range regime ($\alpha \leqslant 1$), $\Delta(k)$ becomes divergent at $k = 0$, leading to the topological singularity in the dispersion which makes the winding vector ill defined at this point [50]. Accordingly, the energy band touching can only occur at $k = \pi$ and the only contribution to the winding number computation from the point $k = \pi$ [73,76]. In this case, the real part of $Z(k)$ is only zero for $k = \pi$, leaving the lines $\mu = 4t \pm \sqrt{V_Z^2 - \Delta^2(\pi)}$ gapped. At point $k = 0$, the real part of $Z(k)$ and the dispersion diverge, where the lines $\mu = \pm\sqrt{V_Z^2 - \Delta^2(0)}$ become gapless. As a consequence, only two distinctive sectors appear in the phase diagram below the critical line $\alpha = 1$.

To determine the winding number for in the long-range regime, we note that the only contribution to the integral in Eq. (A6) comes from the point $k = \pi$. By linearizing the real and imaginary parts of $Z(k)$ at the point $k = \pi$, we have

$$\mathrm{Re}[Z(k)] \sim (4t - \mu)^2 - V_Z^2 + \widetilde{\Delta}^2, \tag{A10}$$

$$\mathrm{Im}[Z(k)] \sim 4t_\lambda(k - \pi)\widetilde{\Delta}, \tag{A11}$$

where $\widetilde{\Delta} = \Delta[1 - (2 - 2^{2-\alpha})\zeta(\alpha)]$ with ζ denoting the Riemann zeta function. The winding number for the case of $\alpha \leqslant 1$ can then be explicitly calculated with numerical methods and its final results are given by

$$W = \frac{1}{2\pi}\int_{-\infty}^{\infty} dk\,\partial_k\varphi(k) = \begin{cases} -\frac{1}{2} & \text{for } |\mu - 4t| < \sqrt{V_Z^2 - \Delta^2(\pi)}, \\ +\frac{1}{2} & \text{for } |\mu - 4t| > \sqrt{V_Z^2 - \Delta^2(\pi)}, \end{cases} \tag{A12}$$

which exactly agrees with the results given by Eq. (10) in the main text.

[1] A. Y. Kitaev, Phys. Usp. **44**, 131 (2001).
[2] J. D. Sau, R. M. Lutchyn, S. Tewari, and S. Das Sarma, Phys. Rev. Lett. **104**, 040502 (2010).
[3] J. Alicea, Phys. Rev. B **81**, 125318 (2010).
[4] R. M. Lutchyn, J. D. Sau, and S. Das Sarma, Phys. Rev. Lett. **105**, 077001 (2010).
[5] Y. Oreg, G. Refael, and F. von Oppen, Phys. Rev. Lett. **105**, 177002 (2010).
[6] D. A. Ivanov, Phys. Rev. Lett. **86**, 268 (2001).
[7] A. Kitaev, Ann. Phys. **303**, 2 (2003).
[8] C. Nayak, S. H. Simon, A. Stern, M. Freedman, and S. Das Sarma, Rev. Mod. Phys. **80**, 1083 (2008).
[9] C. W. J. Beenakker, Annu. Rev. Condens. Matter Phys. **4**, 113 (2013).
[10] S. R. Elliott and M. Franz, Rev. Mod. Phys. **87**, 137 (2015).
[11] V. Mourik, K. Zuo, S. M. Frolov, S. R. Plissard, E. P. A. M. Bakkers, and L. P. Kouwenhoven, Science **336**, 1003 (2012).
[12] A. Das, Y. Ronen, Y. Most, Y. Oreg, M. Heiblum, and H. Shtrikman, Nat. Phys. **8**, 887 (2012).
[13] H. O. H. Churchill, V. Fatemi, K. Grove-Rasmussen, M. T. Deng, P. Caroff, H. Q. Xu, and C. M. Marcus, Phys. Rev. B **87**, 241401(R) (2013).
[14] A. D. K. Finck, D. J. Van Harlingen, P. K. Mohseni, K. Jung, and X. Li, Phys. Rev. Lett. **110**, 126406 (2013).
[15] S. M. Albrecht, A. P. Higginbotham, M. Madsen, F. Kuemmeth, T. S. Jespersen, J. Nyg, P. Krogstrup, and C. M. Marcus, Nature (London) **531**, 206 (2016).
[16] M. T. Deng, S. Vaitiekėnas, E. B. Hansen, J. Danon, M. Leijnse, K. Flensberg, J. Nygård, P. Krogstrup, and C. M. Marcus, Science **354**, 1557 (2016).
[17] E. M. T. Fadaly, H. Zhang, S. Conesa-Boj, D. Car, O. Gül, S. R. Plissard, R. L. M. Op het Veld, S. Kölling, L. P. Kouwenhoven, and E. P. A. M. Bakkers, Nano Lett. **17**, 6511 (2017).
[18] Z. Wang, J. O. Rodriguez, L. Jiao, S. Howard, M. Graham, G. D. Gu, T. L. Hughes, D. K. Morr, and V. Madhavan, Science **367**, 104 (2020).
[19] M. Valentini, F. Peñaranda, A. Hofmann, M. Brauns, R. Hauschild, P. Krogstrup, P. San-Jose, E. Prada, R. Aguado, and G. Katsaros, Science **373**, 82 (2021).
[20] R. Hess, H. F. Legg, D. Loss, and J. Klinovaja, Phys. Rev. B **104**, 075405 (2021).
[21] H. Pan and S. Das Sarma, Phys. Rev. B **105**, 115432 (2022).
[22] S. Shapiro, Phys. Rev. Lett. **11**, 80 (1963).
[23] H.-J. Kwon, K. Sengupta, and V. M. Yakovenko, Eur. Phys. J. B **37**, 349 (2003).
[24] L. Fu and C. L. Kane, Phys. Rev. B **79**, 161408(R) (2009).
[25] L. Jiang, D. Pekker, J. Alicea, G. Refael, Y. Oreg, and F. von Oppen, Phys. Rev. Lett. **107**, 236401 (2011).
[26] D. I. Pikulin and Y. V. Nazarov, Phys. Rev. B **86**, 140504(R) (2012).
[27] L. P. Rokhinson, X. Liu, and J. K. Furdyna, Nat. Phys. **8**, 795 (2012).
[28] D. Laroche, D. Bouman, D. J. van Woerkom, A. Proutski, C. Murthy, D. I. Pikulin, C. Nayak, R. J. J. van Gulik, J. Nygård, P. Krogstrup, L. P. Kouwenhoven, and A. Geresdi, Nat. Commun. **10**, 245 (2019).
[29] A. Fornieri, A. M. Whiticar, F. Setiawan, E. Portolés, A. C. C. Drachmann, A. Keselman, S. Gronin, C. Thomas, T. Wang, R. Kallaher, G. C. Gardner, E. Berg, M. J. Manfra, A. Stern, C. M. Marcus, and F. Nichele, Nature (London) **569**, 89 (2019).
[30] P. San-Jose, E. Prada, and R. Aguado, Phys. Rev. Lett. **108**, 257001 (2012).
[31] D. I. Pikulin and Y. V. Nazarov, JETP Lett. **94**, 693 (2012).
[32] C. Wittig, J. Phys. Chem. B **109**, 8428 (2005).
[33] D. M. Badiane, M. Houzet, and J. S. Meyer, Phys. Rev. Lett. **107**, 177002 (2011).
[34] J. Wiedenmann, E. Bocquillon, R. S. Deacon, S. Hartinger, O. Herrmann, T. M. Klapwijk, L. Maier, C. Ames, C. Brüne, C. Gould, A. Oiwa, K. Ishibashi, S. Tarucha, H. Buhmann, and L. W. Molenkamp, Nat. Commun. **7**, 10303 (2016).
[35] S. Sumita and A. Furusaki, Phys. Rev. B **104**, 205431 (2021).
[36] M. Kompaniiets, O. V. Dobrovolskiy, C. Neetzel, F. Porrati, J. Brötz, W. Ensinger, and M. Huth, Appl. Phys. Lett. **104**, 052603 (2014).
[37] T. O. Puel and O. Viyuela, Phys. Rev. B **100**, 014508 (2019).
[38] D. Vodola, L. Lepori, E. Ercolessi, A. V. Gorshkov, and G. Pupillo, Phys. Rev. Lett. **113**, 156402 (2014).
[39] D. Vodola, L. Lepori, E. Ercolessi, and G. Pupillo, New J. Phys. **18**, 015001 (2015).
[40] X. Cai, J. Phys.: Condens. Matter **29**, 115401 (2017).
[41] A. Alecce and L. Dell'Anna, Phys. Rev. B **95**, 195160 (2017).
[42] A. A. Dutta and A. A. Dutta, Phys. Rev. B **96**, 125113 (2017).
[43] C. Li, X. Z. Zhang, G. Zhang, and Z. Song, Phys. Rev. B **97**, 115436 (2018).
[44] F. Ares, J. G. Esteve, F. Falceto, and A. R. de Queiroz, Phys. Rev. A **97**, 062301 (2018).

[45] U. Bhattacharya and A. Dutta, Phys. Rev. B **97**, 214505 (2018).
[46] S. Lieu, D. K. K. Lee, and J. Knolle, Phys. Rev. B **98**, 134507 (2018).
[47] J. J. Miao, H. K. Jin, F. C. Zhang, and Y. Zhou, Sci. Rep. **8**, 488 (2018).
[48] U. Bhattacharya, S. Maity, A. Dutta, and D. Sen, J. Phys.: Condens. Matter **31**, 174003 (2019).
[49] X. P. Li, C. F. Li, L. C. Wang, and L. Zhou, Int. J. Theor. Phys. **58**, 1590 (2019).
[50] O. Viyuela, D. Vodola, G. Pupillo, and M. A. Martin-Delgado, Phys. Rev. B **94**, 125121 (2016).
[51] I. Mahyaeh and E. Ardonne, J. Phys. Commun. **2**, 045010 (2018).
[52] D. Giuliano, S. Paganelli, and L. Lepori, Phys. Rev. B **97**, 155113 (2018).
[53] S. B. Jäger, L. Dell'Anna, and G. Morigi, Phys. Rev. B **102**, 035152 (2020).
[54] S. Nadj-Perge, I. K. Drozdov, J. Li, H. Chen, S. Jeon, J. Seo, A. H. MacDonald, B. A. Bernevig, and A. Yazdani, Science **346**, 602 (2014).
[55] G. C. Ménard, S. Guissart, C. Brun, S. Pons, V. S. Stolyarov, F. Debontridder, M. V. Leclerc, E. Janod, L. Cario, D. Roditchev, P. Simon, and T. Cren, Nat. Phys. **11**, 1013 (2015).
[56] R. Pawlak, M. Kisiel, J. Klinovaja, T. Meier, S. Kawai, T. Glatzel, D. Loss, and E. Meyer, npj Quantum Inf. **2**, 16035 (2016).
[57] M. Ruby, B. W. Heinrich, Y. Peng, F. von Oppen, and K. J. Franke, Nano Lett. **17**, 4473 (2017).
[58] H. Kim, L. Rózsa, D. Schreyer, E. Simon, and R. Wiesendanger, Nat. Commun. **11**, 4573 (2020).
[59] S. Park, W. Lee, S. Jang, Y.-B. Choi, J. Park, W. Jung, K. Watanabe, T. Taniguchi, G. Y. Cho, and G.-H. Lee, Nature (London) **603**, 421 (2022).
[60] M. Benito, A. Gómez-León, V. M. Bastidas, T. Brandes, and G. Platero, Phys. Rev. B **90**, 205127 (2014).
[61] Z. Z. Li, C. H. Lam, and J. Q. You, Phys. Rev. B **96**, 155438 (2017).
[62] M. Ezawa, Phys. Rev. B **102**, 075424 (2020).
[63] Z. Tao, T. Yan, W. Liu, J. Niu, Y. Zhou, L. Zhang, H. Jia, W. Chen, S. Liu, Y. Chen, and D. Yu, Phys. Rev. B **101**, 035109 (2020).
[64] J. Wu, Z. Wang, Y. Biao, F. Fei, S. Zhang, Z. Yin, Y. Hu, Z. Song, T. Wu, F. Song, and R. Yu, Nat. Electron. **5**, 635 (2022).
[65] N. A. Olekhno, A. D. Rozenblit, V. I. Kachin, A. A. Dmitriev, O. I. Burmistrov, P. S. Seregin, D. V. Zhirihin, and M. A. Gorlach, Phys. Rev. B **105**, L081107 (2022).
[66] F. Pientka, A. Keselman, E. Berg, A. Yacoby, A. Stern, and B. I. Halperin, Phys. Rev. X **7**, 021032 (2017).
[67] D. T. Liu, J. Shabani, and A. Mitra, Phys. Rev. B **97**, 235114 (2018).
[68] A. Bermudez, T. Schaetz, and M. B. Plenio, Phys. Rev. Lett. **110**, 110502 (2013).
[69] P. Jurcevic, B. P. Lanyon, P. Hauke, C. Hempel, P. Zoller, R. Blatt, and C. F. Roos, Nature (London) **511**, 202 (2014).
[70] H. Q. Wang, L. B. Shao, Y. X. Zhao, L. Sheng, B. G. Wang, and D. Y. Xing, Phys. Rev. B **98**, 174512 (2018).
[71] F. Pientka, L. I. Glazman, and F. von Oppen, Phys. Rev. B **88**, 155420 (2013).
[72] O. Viyuela, L. Fu, and M. A. Martin-Delgado, Phys. Rev. Lett. **120**, 017001 (2018).
[73] J.-T. Ren, S.-S. Ke, Y. Guo, H.-W. Zhang, and H.-F. Lü, Phys. Rev. B **103**, 045428 (2021).
[74] C.-K. Chiu, J. C. Y. Teo, A. P. Schnyder, and S. Ryu, Rev. Mod. Phys. **88**, 035005 (2016).
[75] A. P. Schnyder, S. Ryu, A. Furusaki, and A. W. W. Ludwig, Phys. Rev. B **78**, 195125 (2008).
[76] S. Maity, U. Bhattacharya, and A. Dutta, J. Phys. A: Math. Theor. **53**, 013001 (2020).
[77] A. Zagoskin, *Quantum Theory of Many-Body Systems*, 2nd ed., Graduate Texts in Physics (Springer Cham, Berlin, 2014)
[78] E. Perfetto, G. Stefanucci, and M. Cini, Phys. Rev. B **80**, 205408 (2009).
[79] J. Cayao, P. San-Jose, A. M. Black-Schaffer, R. Aguado, and E. Prada, Phys. Rev. B **96**, 205425 (2017).
[80] G. Stefanucci and C.-O. Almbladh, Phys. Rev. B **69**, 195318 (2004).
[81] G. Stefanucci, E. Perfetto, and M. Cini, Phys. Rev. B **81**, 115446 (2010).
[82] J. Cayao and A. M. Black-Schaffer, Phys. Rev. B **104**, L020501 (2021).
[83] J. Cayao, A. M. Black-Schaffer, E. Prada, and R. Aguado, Beilst. J. Nanotechnol. **9**, 1339 (2018).
[84] W. Tan, L. Chen, X. Ji, and H.-Q. Lin, Sci. Rep. **4**, 7381 (2015).
[85] J. Noh, T. Schuster, T. Iadecola, S. Huang, M. Wang, K. P. Chen, C. Chamon, and M. C. Rechtsman, Nat. Phys. **16**, 989 (2020).
[86] B. Xie, H.-X. Wang, X. Zhang, P. Zhan, J.-H. Jiang, M. Lu, and Y. Chen, Nat. Rev. Phys. **3**, 520 (2021).